

Evaluation of the Applicability of IFRA for Short Circuit Fault Detection of Stator Windings in Synchronous Machines

Yueqiang Yu^{ID}, Zhongyong Zhao^{ID}, Member, IEEE, Yu Chen^{ID}, Hanzhi Wu^{ID}, Chao Tang^{ID}, Member, IEEE, and Wenwen Gu^{ID}

Abstract—A machine is a device to realize the mutual conversion of electric energy and mechanical energy. This work mainly discusses the applicability of impulse frequency response analysis (IFRA) to detect the stator winding short circuit faults. The parameters of excitation waveform and signal sampling were carefully selected. A solid-state nanosecond pulsed power source prototype was developed for resonant excitation of windings. The proposed method was then verified on a 5-kVA, 380-V, two-pole, the salient synchronous machine (SM) through artificial fault experiments. Finally, the proposed method was compared with other traditional methods. The method has the advantages of fast measurement, rich high frequencies, high stability, and low cost. Since the principle of IFRA is also applicable to large SMs, this method and device may also be applied to detect large SMs winding short circuit faults. It can be used as an auxiliary and alternative method in the nondestructive fault detection of SMs.

Index Terms—Fault detection, frequency response, measurement, synchronous machine (SM), winding.

I. INTRODUCTION

IN RECENT years, in order to avoid production loss and reduce the possibility of maintenance, the safe operation of machines has attracted extensive attention. Especially for small- and medium-sized synchronous machines (SMs), they can be used as both generators and electric machines and has many applications in the industry. However, short circuit faults of stator windings, common faults of SM, may eventually cause catastrophic failure. The short circuit fault can be divided into interturn short circuit (ITSC), and ground short circuit (GSC) faults. Many factors are responsible for the short circuit failure of the stator winding, for instance, the staff's operation errors, physical damage caused by the transportation process, the poor operating environment, and the lifetime limitation. The slight ITSC fault can be easily overlooked. If it is not processed in time, the entire machine may even be burned down by developing short circuit faults. Therefore,

Manuscript received 8 March 2022; revised 4 August 2022; accepted 12 August 2022. Date of publication 25 August 2022; date of current version 12 September 2022. This work was supported in part by the National Natural Science Foundation of China under Grant 51807166 and in part by the Natural Science Foundation of Chongqing under Grant cstc2019jcyj-msxmX0236. The Associate Editor coordinating the review process was Loredana Cristaldi. (Corresponding author: Zhongyong Zhao.)

The authors are with the College of Engineering and Technology, Southwest University, Chongqing 400716, China (e-mail: zhaozhongyong@cqu.edu.cn). Digital Object Identifier 10.1109/TIM.2022.3201561

accurate detection of the stator winding short circuit fault is significant to the SM safe and reliable operation.

The fault detection technology of machine winding is mainly divided into online and offline. Online detection technology can track and feedback the state of the machine winding in time. However, the dynamic changes in temperature, load, speed, and other conditions during machine operation will lead to changes in electrical parameters. The online detection technology is difficult to reflect the real state of machine winding accurately. In contrast, some existing online detection technologies, such as the current characteristic analysis method [1], [2], [3] and coil detection method [4], need to install current, voltage, magnetic flux, and other sensors on the machine's internal structure. It has high requirements for sensors and machines' installation and insulation performance, which is difficult to achieve. Especially for the machine that has been put into operation, its compact internal structure is difficult to install other sensors.

The offline detection technology is mainly to conduct regular preventive tests on the machine under the condition of machine shutdowns, such as the inductive impedance method [5] and repetitive surge oscilloscope (RSO) [6]. Its advantages are simple operation and fast detection. However, there are still deficiencies in the detection ability of the degree and type of slight short circuit fault. Based on this, frequency response analysis (FRA) has been introduced into the short circuit fault detection of machine windings in recent years. Existing FRA is mainly used to detect the mechanical deformation of power transformer windings because of its fast, sensitive, nondestructive, and easy application features. Uhrig *et al.* [7] suggest that according to the nature of the excitation signal, FRA can be divided into sweep FRA (SFRA) and impulse FRA (IFRA). Platero *et al.* [8], Blazquez *et al.* [9], and [10] Platero use SFRA to detect induction and SM winding ITSC faults. Meanwhile, SFRA is used to detect the rotor fault of a 106 MVA SM, and the effect of stator winding status on the SFRA curve is analyzed [11]. In addition, Uhrig *et al.* [7] use SFRA to detect the damp winding broken rod failure in the SM without disassembling the machine. The results show that the broken rod in the damp winding can cause an obvious deviation in FRA measurement between the rotor and stator. IFRA method is performed when SMs are off the line and during maintenance. Therefore, the method is to inject

nanosecond pulses to excite the winding and thus obtain a high-frequency signal to detect winding faults. According to [12], high-frequency signals are very sensitive to winding minor faults. Any phase of the stator winding that can be represented as an equivalent circuit, composed of resistances, inductances, and capacitors, in series or parallel connection. According to [13], the resonant frequency of the winding is $f = 1/2\pi(LC)^{1/2}$; assuming that the winding state changes, in the high-frequency (HF) band, the effect of the inductance is less than the capacitance due to the skin effect. Thus, the ratio of the resonant frequency f_2 under fault compared with the resonant frequency f_1 without fault when ignoring small changes in inductance L is $f_2/f_1 = 1/(1 + \Delta C/C)^{1/2}$. In turn, the higher frequency band of FRA could characterize the small changes in parameters, namely, the minor fault. However, the upper-frequency limit of conventional SFRA equipment is only 2 MHz. Thus, traditional SFRA may not easily detect minor faults. Meanwhile, SFRA is time-consuming in actual application.

In this context, to provide an alternative, simple, fast, easy, and sensitive method, IFRA is introduced to detect short circuit faults of stator windings in the SM, and the applicability of IFRA is discussed. IFRA can be measured when the machine is in shutdown and maintenance, easily implemented in offline status, especially with condition-based maintenance technique. Besides, IFRA uses the pulse signal with a lower rising time as the excitation signal. The excitation contains rich high-frequency components, which can be sensitive to minor winding faults. At the same time, it has a short measurement time and low requirements for external environmental conditions. IFRA can be an alternative and auxiliary method. The novel contribution of this article is to introduce IFRA into fault detection of SM windings for the first time and demonstrate its applicability from experiments using the statistical index of the first anti-resonance features of IFRA. In addition, an adequate pulse parameter is determined for the exact purpose.

Section II presents the method and principle and carefully selects system parameters. A solid-state pulse source that can excite the windings is then developed and tested in Section III. Section IV studies the rotor's influence on the measurement, and then the experiment and analysis of winding short circuit fault are introduced. Section V discusses the performance of the IFRA method by comparing it with other methods. Finally, the conclusions are presented in Section VI.

II. PRINCIPLE AND SYSTEM PARAMETER SELECTION

A. Method and Principle

At HFs (1 kHz–1 MHz), each slot in the stator can be represented by an equivalent lumped parameter circuit unit composed of resistance, inductance, and capacitance. The magnetic core has a negligible effect [8], [9], [10]. High-frequency signals are more sensitive to minor faults. However, the wiring and other factors could have a noticeable influence on the measurement result. Therefore, the frequencies below 1 MHz are typically analyzed.

The equivalent circuit of the entire stator is a cascade connection of several lumped parameter circuit basic units.

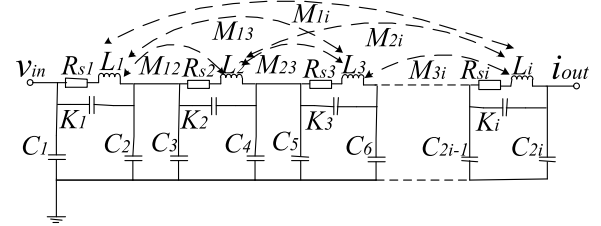


Fig. 1. Schematic of broadband equivalent circuit model of stator winding [14].

Specifically, each basic unit can be seen as one π -type circuit composed of inductance, capacitance, and resistance, as shown in Fig. 1 [14]. R_{si} and L_i represent the resistance and inductance of stator winding, K_i and C_{2i} represent the series capacitance and grounding capacitance, and M_{ni} is the mutual inductance between the n th inductance unit and i th inductance unit. The parameters in the model of Fig. 1 are frequency dependent, and maximum frequency depends on the rise and fall time of the incident pulse wave [15], [16].

Fig. 2 shows a flowchart for evaluating the applicability of IFRA in the stator winding short circuit fault detection. When an excitation pulse signal v_{in} is injected into the winding terminal, the response signal v_{out} or i_{out} can be measured at the other winding terminal. i_{out} is used in this study. Both v_{in} and i_{out} are simultaneously recorded in the time domain. The spectrum components of excitation and response signals are obtained by transforming signals from the time domain to the frequency domain. The fast Fourier transform (FFT) is often used. Finally, the system's transfer function is obtained, and it is usually expressed as $H(\omega)$ [17] in the logarithmic form and expressed in units of decibel. The calculation equations of the transfer function are as follows (1)–(3). The amplitude of $H(\omega)$ at different frequency points represents the IFRA curve. The excitation pulse should have a wide frequency characteristic, and the edges and width of the excitation pulse determine the upper-frequency limit. Therefore, high and wide frequencies should be obtained by setting appropriate parameters of the excitation pulse

$$V_{in}(\omega) = \sum_{n=0}^{N-1} v_{in}(n) e^{-j \frac{2\pi}{N} \omega n} \quad (1)$$

$$I_{out}(\omega) = \sum_{n=0}^{N-1} i_{out}(n) e^{-j \frac{2\pi}{N} \omega n} \quad (2)$$

$$H(\omega) = 20 \log_{10} \frac{|I_{out}(\omega)|}{|V_{in}(\omega)|} \quad (3)$$

where $v_{in}(n)$ is the N points sampled signal of excitation voltage; $i_{out}(n)$ is the N points sampled signal of response current; $V_{in}(\omega)$ and $I_{out}(\omega)$ are FFT of $v_{in}(n)$ and $i_{out}(n)$.

When the stator winding has a slight fault, the structure or electrical parameters of the equivalent circuit will change, and the transfer function will change, according to the nature of the fault [11]. Therefore, it is possible to detect a winding fault and even recognize the fault degree and types by horizontally or vertically comparing the IFRA curves of healthy and faulty winding. The IFRA curve of healthy winding can also be called a “fingerprint.” The vertical comparison means comparing the difference between the IFRA curve

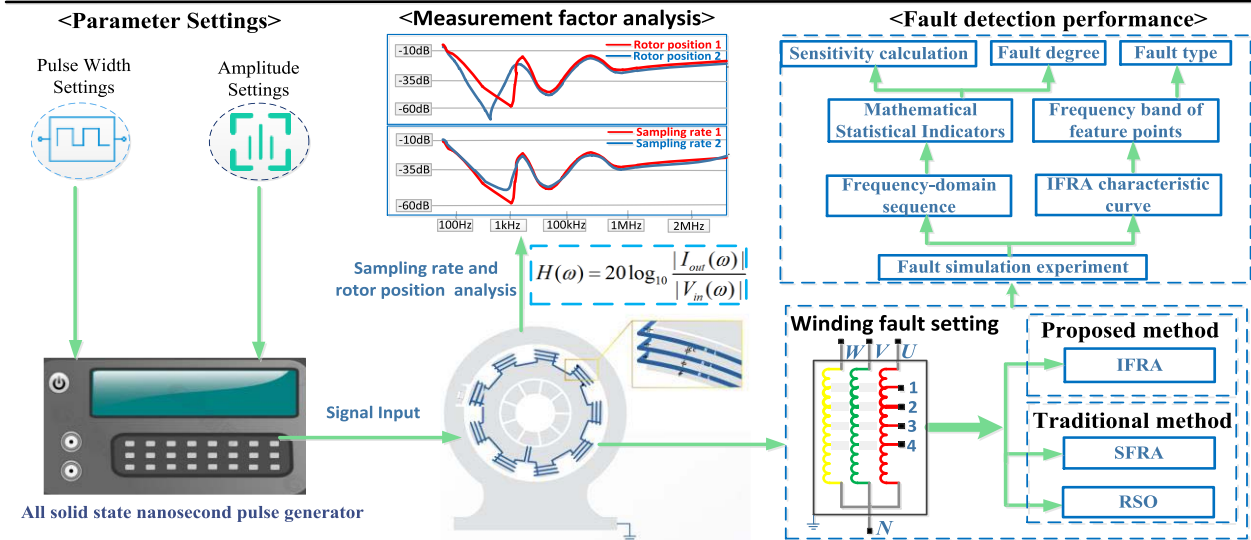


Fig. 2. Flowchart for evaluating the applicability of IFRA in stator winding short circuit fault detection.

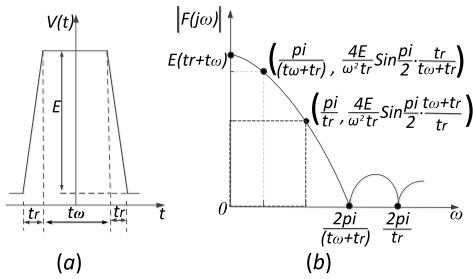


Fig. 3. Time- and frequency-domain waveform of square wave pulses. (a) Time-domain waveform. (b) Frequency spectrum.

of measured winding and its “fingerprint.” The horizontal comparison means comparing the IFRA curve of measured winding with the curves of other phases or other electrical machinery of the same type.

B. Critical Parameters of Excitation Pulse and Signal Sampling

1) *Width of the Excitation Pulse:* The selection of the excitation pulse parameters has a significant impact on the measurement results of the IFRA method, which is described in [18]. We select the square wave pulse to improve the reproducibility and controllability of the excitation impulse signal. Not considering the double exponential voltage, its waveform is significantly affected by the load.

The time-domain waveform of the square wave pulse is shown in Fig. 3(a). The rise time should be considered in the actual square wave pulse. Therefore, set the pulse amplitude is E , the pulsewidth parameter to t_ω , and the rise time parameter to t_r , and the time-domain expression is shown as follows:

$$V(t) = \begin{cases} \frac{E}{t_r} \left(t + t_r + \frac{t_\omega}{2} \right), & -t_r - \frac{t_\omega}{2} \leq t \leq -\frac{t_\omega}{2} \\ E, & -\frac{t_\omega}{2} \leq t \leq \frac{t_\omega}{2} \\ \frac{E}{-t_r} \left(t - t_r - \frac{t_\omega}{2} \right), & \frac{t_\omega}{2} \leq t \leq \frac{t_\omega}{2} + t_r. \end{cases} \quad (4)$$

Equation (4) is processed by FFT, and the expression of its frequency spectrum is expressed as follows:

$$F(j\omega) = \begin{cases} \frac{4E}{t_r \omega^2} \sin \frac{t_r \omega}{2} \sin \frac{(t_r + t_\omega)\omega}{2}, & \omega \neq 0 \\ E(t_\omega + t_r), & \omega = 0. \end{cases} \quad (5)$$

Equation (5) shows that the first zero-crossing point of the frequency spectrum is $\omega_0 = 2\pi/(t_\omega + t_r)$, as shown in Fig. 3(b). The excitation pulse energy is mainly concentrated in $[0, 2\pi/(t_\omega + t_r)]$. The larger the pulsewidth and rise time, the lower the frequency point ω_0 is. To improve the effective frequency range to detect minor winding faults and avoid pseudo resonant points on the IFRA curve induced by ω_0 [19], the main concentration area of the frequency spectrum should be as large as possible. Therefore, the pulsewidth and rise time should be as low as possible. Since the frequency band used in IFRA needs to cover at least $[0, 1]$ MHz, the pulsewidth parameter should not be higher than 1000 ns. We considered the influence of noise and other disturbances in the field test and the pulse generator device; the pulsewidth is selected as no more than 700 ns, and the rise time is less than 50 ns.

2) *Amplitude of Excitation Pulse:* Due to the core loss and dielectric loss of the pulse signal with a frequency component below 2 MHz in the propagation process of the winding, the amplitude of the signal gradually attenuates, and the higher the frequency component attenuates faster. The voltage attenuation can be roughly expressed by (6), U_1 is the initial voltage amplitude of the injected pulse, U_2 is the voltage amplitude at l , l is the total length of winding that the pulse signal propagates along, and δ is the attenuation index

$$U_2 = U_1 e^{-l\delta}. \quad (6)$$

Suppose the amplitude of the excitation pulse signal is not large. In that case, the signal-to-noise ratio (SNR) of the response signal will be very low, and the noise will seriously affect the frequency response curve.

The stator of a 380-V, 5-kVA SM is excited by different pulse signals (amplitude: 2–28 V, pulsewidth: 300 ns). The

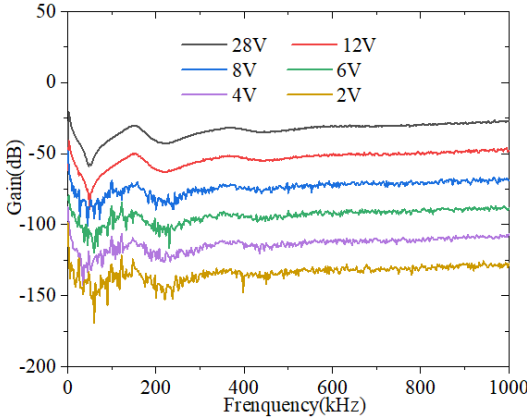


Fig. 4. IFRA curves of stator excited by input different pulse voltage amplitudes.

IFRA curves corresponding to various amplitudes are shown in Fig. 4. A constant value is subtracted from the vertical axis of each curve to separate IFRA curves, and better show their difference. In Fig. 4, when the pulse amplitude is less than 12 V, the noise affects the IFRA curve. Therefore, the lowest pulse amplitude is suggested as 12 V in this study. Although the selection of this amplitude is the experimental result on a simulated experimental machine, the variation law of this amplitude applies to other power machines, but the selection of amplitude will be different. In practical application, if there is large noise in the IFRA curve, the impulse amplitude should be increased appropriately.

Due to the equivalent circuit model of SM being a linear system, the variation of the upper amplitude of excitation will not change the IFRA of the machine unless the core is saturated under excitation voltage. However, the high voltage will induce insulation problems for the turn-to-turn and grounding insulation. According to [20], [21], a pulse signal (rise time: 200 ns, pulselength: 1 μ s) is injected into the twisted pair (diameter: 1.45 mm) of the machine. The results show that when the voltage reaches 1.2 kV, the probability of partial discharge (PD) of the twisted pair is close to 100%. Thus, the excitation voltage should be less than several kilovolts. To keep a certain margin, we roughly and preliminary provide a suggested voltage. The maximum pulse amplitude is recommended to be 500 V. In engineering applications, the amplitude of the excitation pulse signal may be different for machines of other rated power. However, the suggested amplitude can still be referenced for machines of similar power ratings.

3) Key Parameters of Signal Sampling: According to the Nyquist sampling theorem, the sampling rate should be more than two times the upper frequency of the analyzed signal to ensure that the signal amplitude is not significantly distorted. In engineering, however, this value can reach ten times. This study sets the sampling rate and acquisition points to 25 Msps and 10 000 points. The parameter requirements for pulses are shown in Table I.

III. DESIGN AND IMPLEMENTATION OF A SOLID-STATE NANOSECOND PULSE SOURCE PROTOTYPE

For the first time, this article introduces IFRA to detect the SM winding fault. And there is no low-cost

TABLE I
PARAMETER REQUIREMENTS FOR EXCITATION PULSE
AND SAMPLING SELECTION

Pulse and sampling parameters	Recommended values
Pulse Amplitude(V)	12-500
Pulse Width(ns)	≤ 700
Rising Time (ns)	≤ 50
Sampling Rate (Msps)	25
Sample Points	10000

commercial nanosecond pulse generator specifically designed for SM winding fault detection, which also matches the above-suggested pulse parameters. Therefore, this article designs and manufactures a solid-state nanosecond pulse source prototype. According to Section II, the output pulses of the pulsed power source are designed as adjustable parameters. Pulse amplitude: 0–3 kV, pulselength: 0–1000 ns, repetition frequency: 1–1000 Hz. The pulsed power source comprises Marx's main circuit, high voltage power module, power MOSFET driving module, and control module. The circuit schematic is shown in Fig. 5.

The working principle of the pulsed power source is as follows. First, the control module transforms the original trigger pulse signal generated by the signal generator into four synchronous trigger signals. Because the optical fiber has the advantages of anti-interference between the heavy-current and weak-current parts, the optical fiber and optical fiber connector (HFBR-1414TZ and HFBR-2414TZ) is selected as the isolation and medium to transfer the trigger signals to the power MOSFET driving module. Second, the power MOSFET driving module mainly amplifies the signal through the driver chip to control MOSFETs' switching, which adjusts the pulselength and repetitive frequency of the final output pulse. Besides, the high voltage power module controls the power supply of the Marx circuit by adjusting the parameters on the PC to control the amplitude of the final output pulse. Some virtual devices and parameters are selected as follows.

A. Capacitor of Marx Circuit

The Marx main circuit consists of four-stage charging capacitors, whose capacitance value C_0 must satisfy (7). 941C12P47K is selected as the energy storage capacitance

$$C \leq \frac{\tau V_0}{\Delta V_d R_{\text{load}}} \quad (7)$$

where C is the equivalent series capacitance of four stages, $C_0 = 4C$, τ is the maximum pulselength, V_0 is the amplitude of output pulse voltage, V_d is the allowable falling amplitude of output pulse voltage, which is generally 5%–10%, and R_{load} is the load resistance.

1) MOSFET and Fast Recovery Diode: In the Marx circuit, IXFX26N120P is selected as the MOSFET switch to control the pulse power supply to generate the pulse signal of nanosecond pulse rise time and pulselength. Besides fast recovery diode functions as the isolation between two stages in the Marx circuit, we choose DSE160-12A as a diode. The forward current and reverse breakdown voltage of the diode should

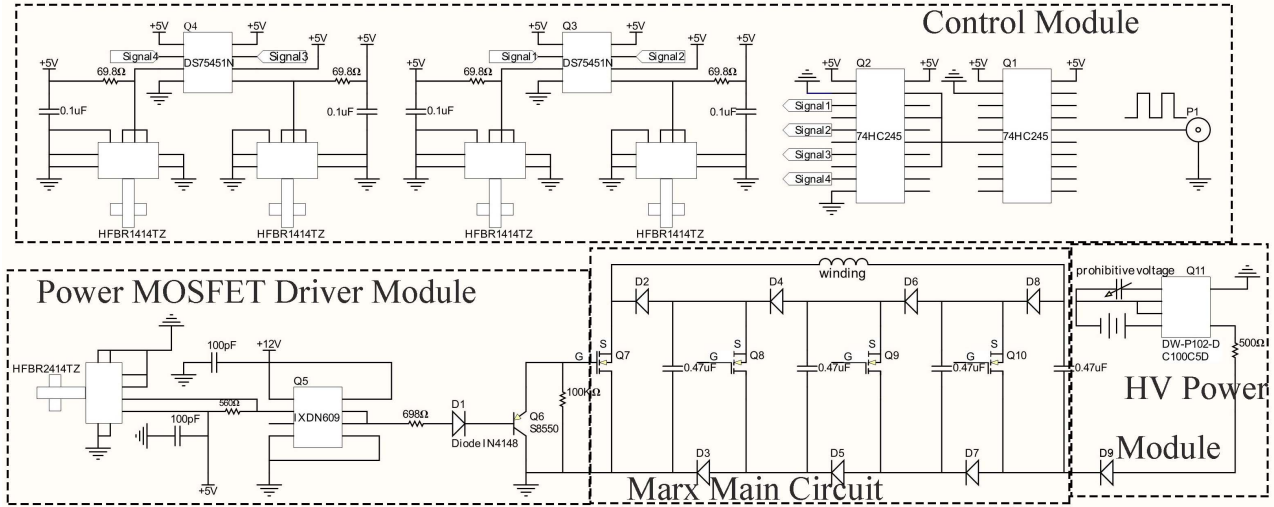


Fig. 5. Circuit schematic of nanosecond pulsed power source prototype.

meet the relationship as shown in the following equation:

$$\begin{cases} V > V_{\max} \\ I > I_{\max} \end{cases} \quad (8)$$

where V_{\max} is the maximum voltage of a capacitor when the Marx circuit is in discharging mode, I_{\max} is the maximum current that flows through the fast recovery diode when the Marx circuit is in charging mode, and V and I are the reverse breakdown voltage and forward current for the fast recovery diode.

2) *Chips and High Voltage Power Module*: The 74HC245 is selected to transform one trigger signal into four signals and improve the driving ability. The DS75451N is a dual and peripheral gate driver, and it is chosen to keep the output multiple trigger signals consistent. The IXDN609 has a high current output and short rise time, especially suitable for driving MOSFET. The DW-P102-DC100C5D is selected to adjust the output voltage linearly.

Fig. 6 shows the performance of the pulse device, including pulse amplitude adjustment and pulselength adjustment experiments. In Fig. 6(a), the pulse amplitude can be variable from 200 to 2500 V. The rise time of nanosecond pulse is within 40 ns. Besides, Fig. 6(b) shows that the width of the pulse signal can be continuously adjusted from 200 to 1000 ns.

IV. EXPERIMENT AND ANALYSIS OF WINDING SIMULATED SHORT CIRCUIT FAULTS

This section artificially simulated the winding short circuit faults on the salient SM (rated power: 5 kVA, rated voltage: 380 V, pole pairs: 1, number of slots: 36) mentioned. First, the influence of rotor position on the IFRA signature of the stator winding is investigated. Second, the short circuit fault of the winding is simulated, three terminals were led out from the wires in slots #2, #3, and #4 of the stator phase-U winding, and the turns that correspond to the three terminals are 4%, 8%, and 12% of entire turns, respectively. The test connection diagram of the IFRA method is shown

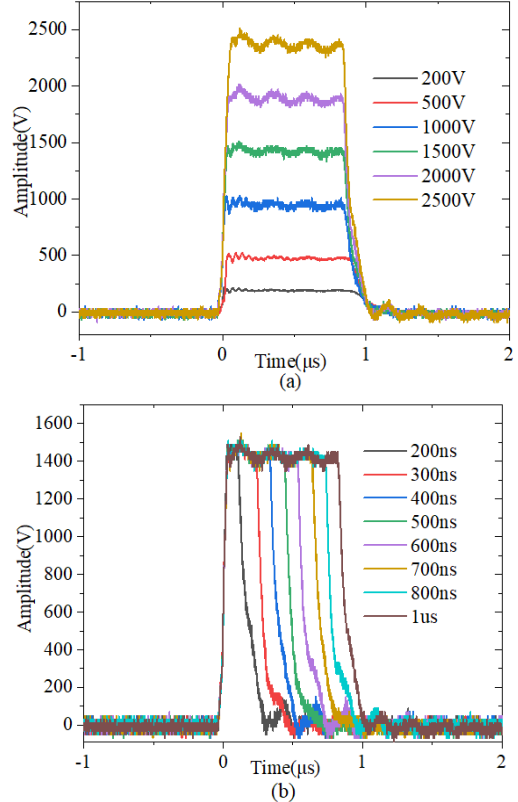


Fig. 6. Performance test of pulsed source. (a) Continuous adjustment of pulse amplitude. (b) Continuous adjustment of pulselength.

in Fig. 7. The excitation voltage and response current are measured by a broadband voltage probe (Tektronix P5100A, bandwidth: 500 MHz) and a current sensor (Pearson, model: 150, bandwidth: 40 Hz–20 MHz, sensitivity: 0.5 V/A). The waveforms are recorded by Tektronix MDO4104C oscilloscope (bandwidth: 1 GHz). The IFRA tests were conducted several times in the same state of machinery. Both excitation and response signals of 64 measurements were averaged to

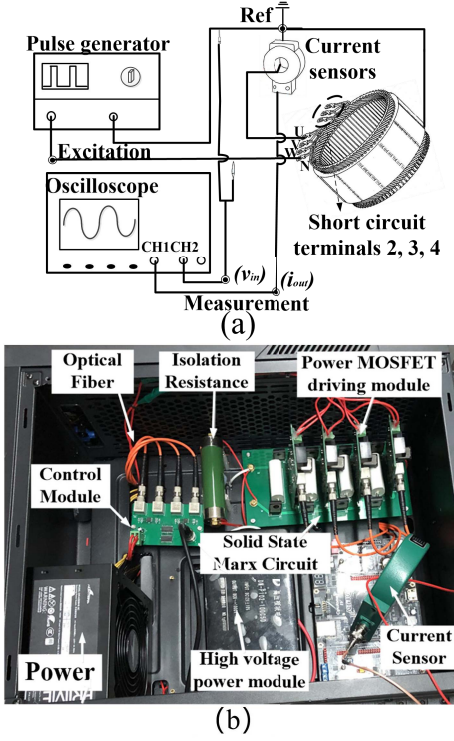


Fig. 7. Test connection diagram of IFRA method. (a) IFRA connection diagram. (b) Field image of test diagram for IFRA method.

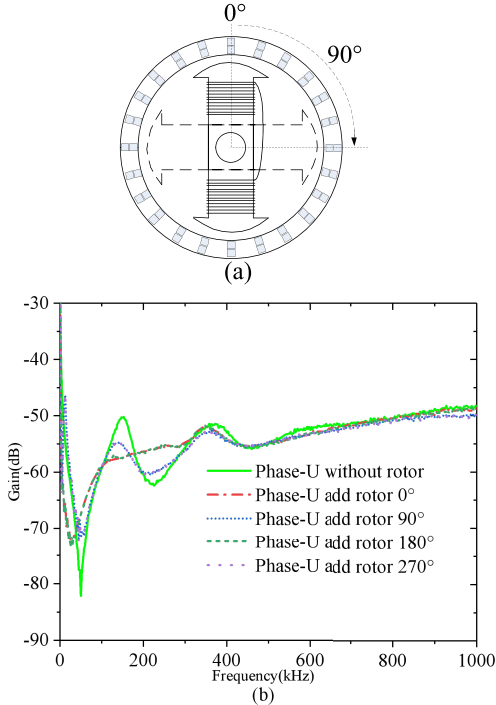


Fig. 8. Schematic of rotor and IFRA curve. (a) Rotation direction of rotor for two-pole machines. (b) Influence of rotor position on IFRA curves of stator winding.

reduce the influence of white noise on measurement. The averaged signals functioned as the time-domain signals for analysis.

TABLE II
INFLUENCE OF ROTOR POSITION ON RF OF IMPULSE FREQUENCY RESPONSE CURVE FOR STATOR WINDING

Experimental Cases	Relative factor (R_{xy})		
	LF	MF	HF
(without rotor) and (rotor 0°)	0.3709	0.2662	1.4442
(without rotor) and (rotor 90°)	0.1763	0.8612	1.1891
(without rotor) and (rotor 180°)	0.3608	0.2674	1.5344
(without rotor) and (rotor 270°)	0.1711	0.8715	1.1733

A. Influence of Rotor Position on IFRA Signature of Stator Winding

For salient poles SM, the position of the rotor may influence the frequency response curve. Therefore, the effect of rotor position on the IFRA signature of stator winding was tested and analyzed. First, we measured the IFRA signature of the stator winding without a rotor. Second, a slot of the stator core was marked as the initial position, and the rotor was installed under different angles concerning the initial position, including 0°, 90°, 180°, and 270°, respectively, simulating different situations of the rotor. The rotation direction of the rotor is shown in Fig. 8(a). The IFRA curves of stator phase-U winding measurement results are shown in Fig. 8(b). To carry out the quantitative analysis of variable IFRA curves, we refer to the Chinese power industry standard DL/T911, which is used for FRA of power transformers. Relative factor (RF) R_{xy} is used. The formula for calculating R_{xy} [22] is shown in (9)–(12) and the R_{xy} in (10) evaluates the similarity of the two frequency response curves (X_i and Y_i). [23] suggests that 1–100 kHz is the low frequency (LF) band, 100–600 kHz indicates the medium frequency (MF) band, and 600–1000 kHz represents the HF band. Although the frequency division method is used for FRA analysis of transformer, it can still be used for reference in machine analysis. The RF is calculated and shown in Table II

$$D_x = \frac{1}{N} \sum_{i=1}^N \left(X_i - \frac{1}{N} \sum_{i=1}^N X_i \right)^2 \quad (9)$$

$$D_y = \frac{1}{N} \sum_{i=1}^N \left(Y_i - \frac{1}{N} \sum_{i=1}^N Y_i \right)^2 \quad (10)$$

$$C_{xy} = \frac{\frac{1}{N} \sum_{i=1}^N \left(X_i - \frac{1}{N} \sum_{i=1}^N X_i \right) \times \left(Y_i - \frac{1}{N} \sum_{i=1}^N Y_i \right)}{\sqrt{D_x D_y}} \quad (11)$$

$$R_{xy} = \begin{cases} 10, & 1 - C_{xy} < 10^{-10} \\ -\log_{10}(1 - C_{xy}), & \text{otherwise} \end{cases} \quad (12)$$

where X_i and Y_i are sequences of length N , $i = 0, 1, 2, \dots, N-1$, D_x and D_y are the standard variance, and C_{xy} is the normalized covariance coefficient.

As shown in Fig. 8(b) and Table II, the value of R_{xy} is less than 0.5 and 1 in LF and MF bands, respectively. There is a significant difference between IFRA curves corresponding to the rotor's presence or absence. The R_{xy} corresponding to different rotor positions shows a significant difference. The

reasons are as follows: the rotor will change the equivalent electrical parameters of the stator, and the variation of the air gap and magnetic flux is more significant. Thus, the inductive region of the IFRA curve possessed a considerable change. The rotor's different positions will change the parameters of the stator, especially the inductance, which will undoubtedly change the IFRA curves. Also, in frequency ranges below 600 kHz, the inductance and capacitance are dominant, and the variations of IFRA curves are significant. In HF (> 600 kHz), the flux penetration into the core is neglected, and the effect of the rotor is insignificant. Thus, the IFRA curves are unchanged.

However, the value of R_{xy} is close between 0° and 180° , and the R_{xy} value corresponding to 90° and 270° are close. Because the machine is a geometric symmetrical structure, the IFRA curves of winding with the rotor of 0° and 180° and 90° and 270° , almost coincide, respectively. Therefore, the rotor positions have a significant influence on the IFRA curve of the stator. The rotor position should be marked and fixed for each experiment when the IFRA method is applied in practice.

B. ITSC Fault Test of Stator Winding

We shorten terminals #2 and #3 and #2 and #4 to simulate the ITSC fault. The IFRA curves of the phase-U were then measured. Besides, the ITSC fault will reduce effective turns, and the equivalent series inductance of the electrical model has decreased [23]. Thus, we simulate this fault by changing series inductance to obtain more data on ITSC fault. The first step is to estimate the equivalent inductance of winding. The winding impedance mainly determines the inductance L at LF, and the inductance can be calculated by ($L = |Z| \sin \theta / 2\pi f_{low}$), where Z is the impedance in the low-frequency band, f_{low} and θ is the frequency and phase angle [24]. Thus, the phase-U impedance curve was measured by a Keysight impedance analyzer (E4900A), shown in Fig. 9. We calculated some inductances using several points in the low-frequency band and found that the inductances are approximately equal. Thus, we randomly selected eight points on the impedance curve in the low-frequency band and calculated the average value, as shown in Fig. 9(b). The equivalent inductance of one turn is estimated to be $112 \mu\text{H}$. However, artificially decreasing the series inductance of winding is challenging to implement; this article, in turn, simulates such an effect by paralleling an inductance to two terminals. This protocol also verifies that the winding ITSC will affect the series inductance. The inductance of 10 and $100 \mu\text{H}$ is connected to terminals #2 and #3. Finally, we measured the IFRA curve under each situation, and raw time-domain waveforms and IFRA curves of ITSC fault are shown in Fig. 10. Table III presents the RF.

In Fig. 10(b), the changing trend of the IFRA curves in the low-frequency band is approximately the same for different cases. In Table III, for indirect and artificial short circuit fault, the frequency shift of first anti-resonance is as high as 10.55% , not to mention the direct short circuit fault, which demonstrates that IFRA shows a high sensitivity. Besides, with the increase of the fault degree, the curves are shifted to the high-frequency band. The larger the fault degree, the

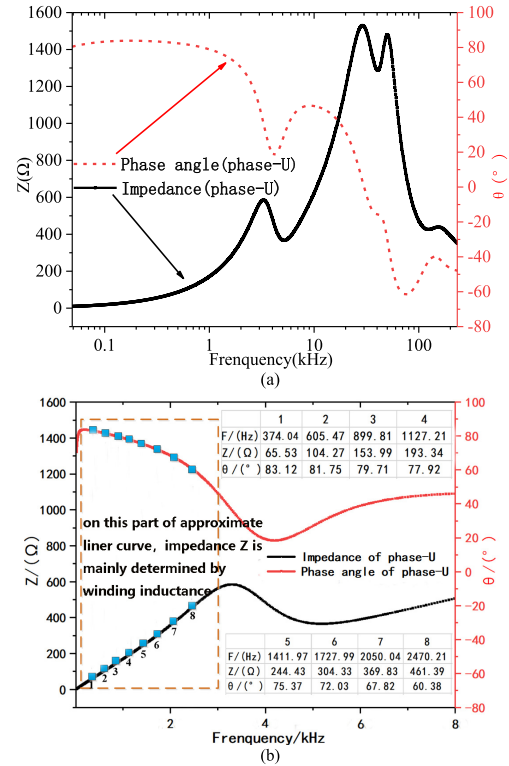


Fig. 9. Impedance characteristic curve of stator phase-U winding. (a) Impedance characteristic curve of phase-U winding in [0–5] MHz. (b) Impedance characteristic curve of phase-U winding in [0–8] kHz.

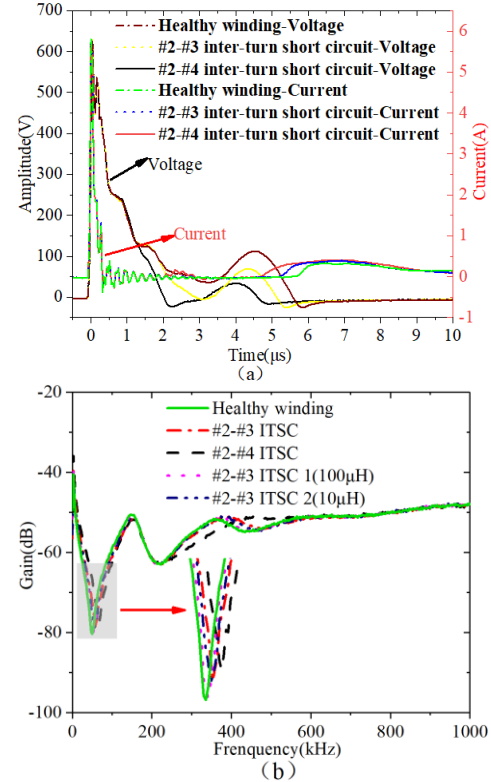


Fig. 10. Raw time-domain waveforms and IFRA curves of ITSC fault. (a) Raw time-domain waveforms. (b) IFRA curve.

larger the extent of IFRA curve variation. This phenomenon can be explained based on ($f = 1/2\pi(LC)^{1/2}$), where L is the impedance and C is the capacitance. The inductance

TABLE III
RF AND FREQUENCY SHIFT OF FREQUENCY RESPONSE
CURVES OF ITSC FAULT

Experimental Cases	Relative factor (R_{xy})			Frequency shift of first anti-resonance
	LF	MF	HF	
2-3 ITSC (100 μ H)	2.9513	2.0432	1.5441	10.55%
2-3 ITSC (10 μ H)	2.2829	1.3505	1.6429	15.81%
2-3 ITSC	1.6497	1.0857	1.6457	21.07%
2-4 ITSC	1.8280	0.6792	1.4287	42.13%

TABLE IV
RF AND FREQUENCY SHIFT OF FREQUENCY RESPONSE
CURVE OF GSC FAULT

Experimental Cases	Relative factor (R_{xy})			Frequency shift of first anti-resonance
	LF	MF	HF	
GSC fault	0.1836	0.1259	1.2132	-3.01%
GSC fault (20 Ω)	0.1488	0.3654	1.4239	-5.41%
GSC fault (40 Ω)	0.1328	0.3389	1.3479	-11.28%
GSC fault (60 Ω)	0.1012	0.3647	1.3794	-22.01%

mainly determines the resonant frequency if the resistance is ignored and the effect of capacitance is not significant, at least less than the change of inductance. The winding inductance decreases gradually with the increase of ITSC fault extent and the corresponding resonant frequency increases.

C. GSC Fault Test of Stator Winding

The GSC fault is also one of the common fault types in the machine. This article also experimentally simulates and analyzes the GSC fault of the stator winding. First, terminal #2 of the stator phase-U winding was directly grounded, and the IFRA curve was measured. Second, the resistance of 20, 40, and 60 Ω is connected in series to the grounding wire, respectively, to simulate different fault degrees. The corresponding IFRA curves were measured. The raw time-domain waveforms and IFRA curves are shown in Fig. 11. The RF is shown in Table IV.

As shown in Fig. 11(b) and Table IV, the IFRA curves of GSC faults are significantly different from healthy winding, especially in LF and MF bands. Besides, the first anti-resonance of the IFRA faulty curve is shifted to the LF band, and simultaneously, the GSC leads to a large increase in the gain of the first anti-resonance point. With the increase of GSC fault resistance, the gain of the first anti-resonance point decreases. In addition, it can be seen from Figs. 10(b) and 11(b) that the changes of the first anti-resonance point caused by different faults are different so that IFRA can distinguish different types of short circuit faults.

After the ITSC and GSC fault experiments, the results show that the frequency characteristic points of ITSC and GSC fault are concentrated below 1 MHz. However, there are many types of faults in SM. Whether the range of other fault types or more

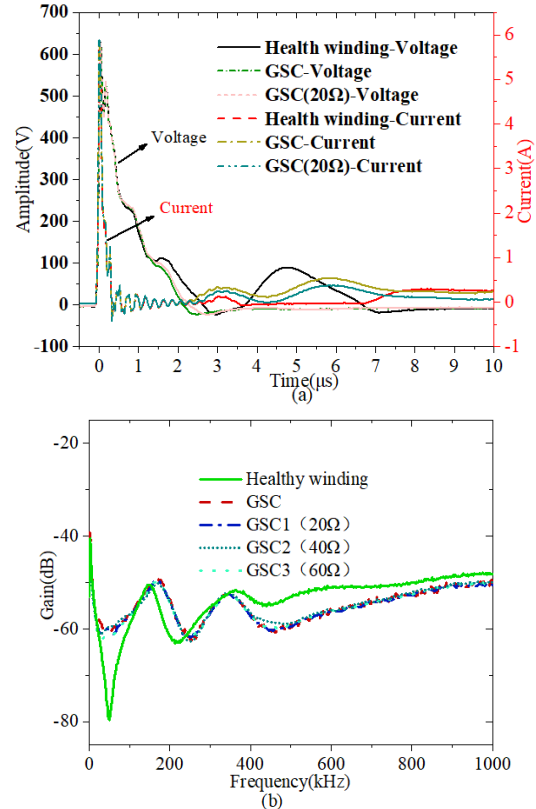


Fig. 11. Raw time-domain waveforms and IFRA curves of GSC fault. (a) Raw time-domain waveforms. (b) IFRA curve.

minor fault feature points is greater than 1 MHz needs to be further studied.

V. COMPARISON OF IFRA METHOD WITH OTHER METHODS

To verify the performance of the IFRA method, it is compared with traditional SFRA and RSO.

A. Comparison of IFRA With SFRA Method

First, we used a commercial FRA analyzer (model: SFRB-R, sweep frequency range: 10 Hz–2 MHz, repetition rate of same phase test: 99.5%) to measure the SFRA curve of each phase winding, respectively. Fig. 12 shows the comparison of SFRA and IFRA signatures for three-phase stator winding. It can be seen that there is a constant difference between the SFRA and IFRA signatures of the same phase, which is because the nature of response signals for the two methods are different. For IFRA, the IFRA curve is the ratio of the response current to excitation voltage, namely, the transfer admittance. However, for SFRA, the response signal is the voltage on the output impedance of 50 Ω (cable); the SFRA curve is a voltage ratio. Thus, the constant difference of gain is $20 \log_{10}(50) = 34$ dB in the entire frequency range. Besides, the IFRA curve corresponds to the SFRA curve. Therefore, the status of winding can be characterized by the IFRA signature, and the developed nanosecond pulse source is feasible for exciting the resonant points of IFRA curves.

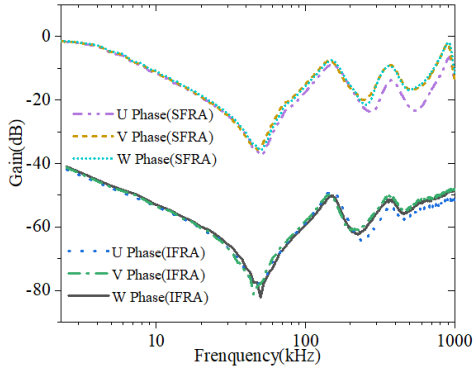


Fig. 12. Comparison of SFRA and IFRA method for three-phase stator.

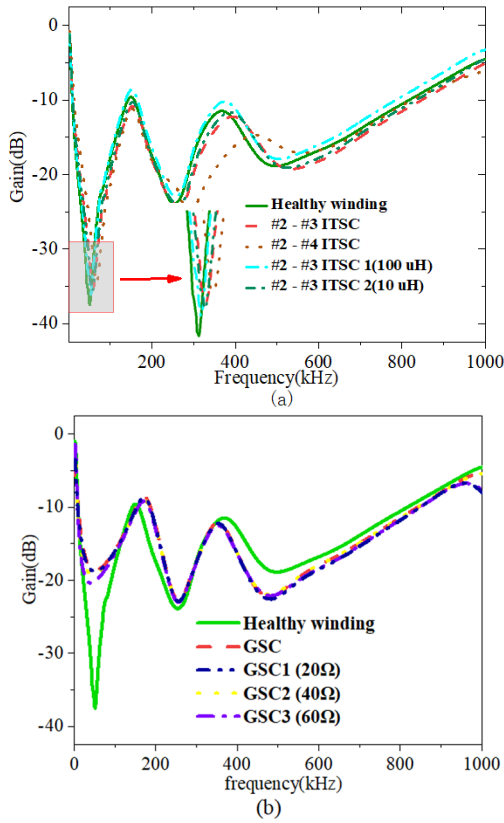


Fig. 13. SFRA curves corresponding to the ITSC and GSC faults. (a) ITSC fault test. (b) GSC fault test.

For simplicity, the repeatability result of SFRA is not shown in this study. However, high repeatability is foreseeable, referring to the nameplate of the SFRA instrument. In Fig. 12, the variation trend of the IFRA and SFRA curves is consistent. The trend of the curves obtained by the two methods is the same.

To further compare the performance of IFRA and SFRA, we also simulate and test the ITSC and GSC faults with SFRA, the experimental results are shown in Fig. 13. The RF is shown in Table V.

It can be seen from Figs. 13(a) and 10(b) that the trend of the frequency response curve of ITSC faults with different degrees is consistent. With the increase of fault degree, the first

TABLE V
RF AND FREQUENCY SHIFT OF SFRA OF ITSC AND GSC FAULT

Experimental Cases	Relative factor (R_{xy})			Frequency shift of first anti-resonance
	LF	MF	HF	
2-3 ITSC (100μH)	2.1022	2.2922	4.6502	5.88%
2-3 ITSC (10μH)	1.1953	1.3583	3.7271	13.72%
2-3 ITSC	1.0532	1.1548	3.7858	17.64%
2-4 ITSC	0.5864	0.2941	2.5569	33.3%
GSC fault	0.9571	0.6977	3.7640	-1.96%
GSC fault (20 Ω)	0.8752	0.7214	3.6971	-3.90%
GSC fault (40 Ω)	0.8658	0.7304	2.2837	-5.88%
GSC fault (60 Ω)	0.9431	0.6894	2.1597	-19.61%

TABLE VI
SENSITIVITY (S) INDEX OF SFRA AND IFRA UNDER WINDING FAULT

Method (fault type)	$S (R_{xy})$			S (Frequency shift of first anti-resonance)
	LF	MF	HF	
IFRA (ITSC)	-0.4003	-0.4357	-0.0343	10.0000
SFRA (ITSC)	-0.4689	-0.6198	-0.6221	8.6180
IFRA (GSC)	-0.0263	0.0690	0.0423	-6.2870
SFRA (GSC)	-0.0051	-0.0016	-0.6226	-5.4930

characteristic frequency point moves toward HF. In addition, from Tables III and V, the changing trends of the R_{xy} and frequency shift of the first characteristic points are consistent for both methods. However, the values of R_{xy} and frequency shift of the first anti-resonance are different due to the different wiring of IFRA and SFRA.

Meanwhile, as shown in Figs. 13(b) and 11(b), the frequency response curves of IFRA and SFRA are also similar. In order to compare the sensitivity of IFRA and SFRA to the same fault, the sensitivity (S) index is used to evaluate and calculate the relationship between the index and the quantitative fault degree (X). S is obtained by fitting each statistical index value with the quantitative value of fault degree through the least square method. The Equation is shown in (13). X represents the quantitative degree (the quantitative degree of each fault type X is quantified as 1, 2, 3, and 4, respectively), and Y represents the index value. The calculation results are shown in Table VI.

As can be seen from Table VI, S is a negative number, indicating a negative correlation between the index and the fault degree. Since the S value of the first anti-resonance is larger than that of R_{xy} , the priority of analyzing the frequency change rate of feature points should be greater than R_{xy} for the judgment of fault degree. Although the R_{xy} and frequency shifts of the first characteristic point of SFRA and IFRA are not similar, it can be seen that the sensitivity S of the two methods is relatively close. So, SFRA and IFRA methods have similar performance in fault detection. Both methods can detect short circuit faults

$$S = \frac{\overline{XY} - \overline{X} \cdot \overline{Y}}{\overline{X^2} - (\overline{X})^2}. \quad (13)$$

B. Comparison of IFRA With RSO Method

The basic principle of RSO is to inject two identical high-frequency pulse waves from both ends of the winding and then calculate the difference between the two response

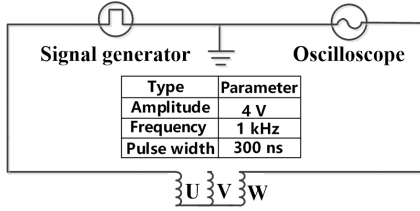
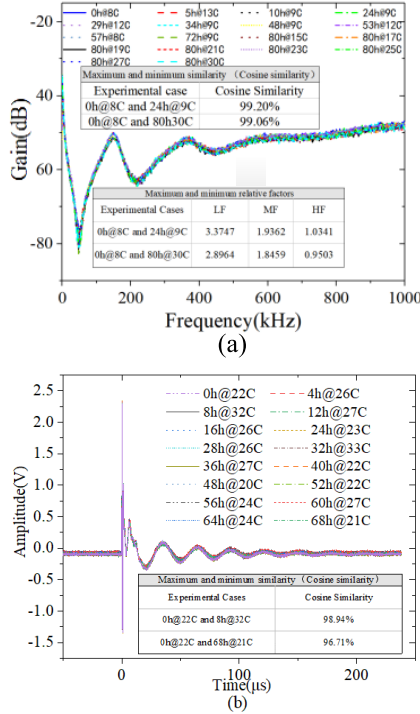


Fig. 14. Connection of RSO test and pulse signal parameter setup.

Fig. 15. IFRA and RSO curves of stability test at different times and ambient temperatures. (a) IFRA stability test. (b) RSO stability test. The term “*h*” means the hours experienced after the first measurement. The term “*C*” means the centigrade of ambient temperature when the measurement was conducted.

waveforms to obtain the “characteristic curve.” Whether the “characteristic curve” shows a bulge is used as the basis of fault detection. First, the stability experiments of the IFRA and RSO methods were carried out. The connection between the RSO test and pulse signal parameter setup is shown in Fig. 14. Variable ambient temperatures are set by performing tests under different conditions, such as in the morning, afternoon, or in an air-conditioned room. The cosine similarity indicator is used to calculate the similarity of the two curves. Fig. 15 shows the IFRA and RSO curves of the stability experiment.

In Fig. 15(a), the IFRA curves measured at different periods and ambient temperatures are coincident, which indicates that the proposed IFRA method is applicable in engineering. In Fig. 15(b), the cosine similarity indicator of RSO is not as high as that of the IFRA method. Second, referring to the experiment setup in Figs. 10 and 11, the RSO experiment is carried out under different winding fault situations. In each state, the pulse signals are injected into phase-U and phase-W, respectively, and then the response curves of the two measurement modes are subtracted to obtain the RSO feature

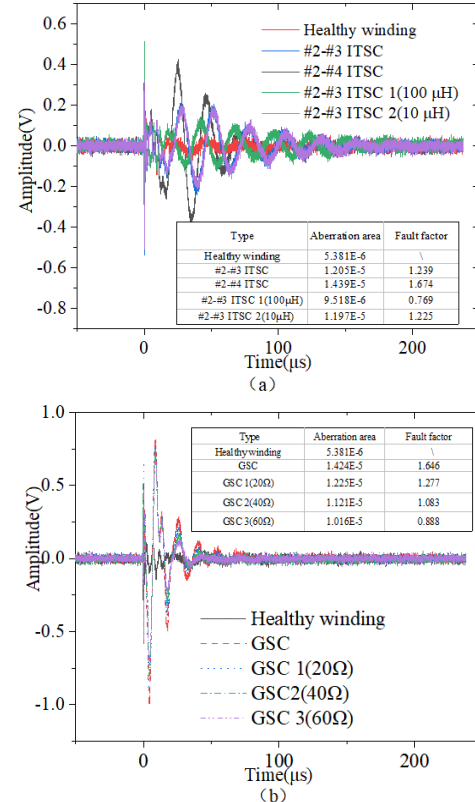


Fig. 16. RSO feature waveforms correspond to different fault types and degrees. (a) Winding ITSC fault. (b) Winding GSC fault.

TABLE VII
SENSITIVITY (*S*) INDEX OF RSO UNDER WINDING FAULT

Fault type	<i>S</i> (Fault factor)
ITSC	0.2729
GSC	-0.2468

waveforms. The aberration area of the RSO feature waveform is used as the fault factor to characterize the fault severity. Fig. 16 shows the result. Table VII shows the sensitivity calculation results.

In Fig. 16, the more serious the fault, the larger the aberration area. It can be seen in Table VII that the sensitivity of RSO to detect ITSC and GSC faults is lower than IFRA and SFRA. In addition, it is difficult to directly recognize the winding fault type from the time-domain waveforms of Fig. 16.

C. Performance Summary of Three Methods

We compare the performance of IFRA, SFRA, and RSO methods. The detection time, cost, repetition rate, sensitivity, and fault detection of there are discussed and summarized. Since the *S* of frequency shift of first anti-resonance points is better than the correlation coefficient R_{xy} , frequency shift of first anti-resonance points is selected to represent the *S* of IFRA and SFRA. The performance parameters are shown in Table VIII.

As shown in Table VIII, IFRA and RSO have advantages over SFRA in cost and detection time. Still, it cannot be ignored that the high stability of SFRA makes it stable for application on important occasions. Meanwhile, IFRA and

TABLE VIII
COMPARISON OF PERFORMANCE INDEXES OF IFRA, SFRA, AND RSO

Performance Parameters	Methods		
	IFRA	SFRA	RSO
Detection time	≈ 1 s	30 s-60 s	≈ 1 s
Stability	99.06%	99.50%	96.71%
Upper frequency limit	>2 MHz	≤ 2 MHz	/
Cost	$\leq \$ 2000$	$\geq \$ 5000$	$\leq \$ 2000$
ITSC fault detection sensitivity	10.0000	8.6180	0.2729
GSC fault detection sensitivity	-6.2870	-5.4930	-0.2468
Fault type identification	High	High	Moderate

SFRA have advantages over RSO in fault type identification and fault degree. The larger upper-frequency limit of IFRA makes it a more promising method for detecting incipient and minor winding faults. In summary, IFRA can be used as an auxiliary and alternative method in the nondestructive fault detection of SM. Further work is in progress to detect different types of SM and verify the generalization of the IFRA.

VI. CONCLUSION

In this article, a detection method of winding short circuit fault of SM based on IFRA is proposed for the first time. To evaluate the applicability of IFRA for stator winding short circuit fault detection, a nanosecond pulse power source for stator winding short circuit fault detection of small- and medium-sized SM is designed and manufactured. The high-voltage nanosecond pulse generated by the pulse power source is regarded as a high-frequency excitation to the machine winding. In response to the current of the machine winding, the IFRA curve is obtained to detect the state of the winding fault. The main conclusions are as follows.

- For the tested 5-kVA machine, this study provides a suggested value for the pulselwidth and amplitude of the excitation signal, which is 100–700 ns and 12–500 V, respectively. This amplitude can still be referenced for machines of similar power ratings. At the same time, A low-cost, adjustable, solid-state nanosecond pulsed power source prototype is designed and implemented in this article. The nanosecond pulses with parameters of 0–3 kV, 100–1000 ns, and 1–1000 Hz can be controlled and produced by the homemade high voltage pulsed source.
- The position of the rotor can significantly affect the stator winding IFRA. The position of the rotor changes the inductance and capacitance parameters of the equivalent circuit of the stator winding. Therefore, when comparing IFRA detection data with reference data, it is necessary to consider whether the rotor position is consistent.
- The fault experiment results verify that the stator's ITSC and GSC faults can be successfully detected by IFRA. Among them, for the minimum ITSC and GSC faults simulated in this article, the offset between IFRA curve and reference data is 10.55% and 89.50%, respectively, indicating that IFRA has high sensitivity. The frequency response characteristics of hundreds of kilohertz frequency bands can effectively reflect the degree and type

of SM winding short circuit fault, which has practical engineering potential.

- Compared with SFRA and RSO, IFRA has a fast inspection speed (less than 1 s), low cost (less than \$2000), and high sensitivity. In addition, IFRA has rich high-frequency signals (larger than 2 MHz), which can detect more minor faults. It can be used as an alternative method in the fault detection of SM.

REFERENCES

- A. Sadeghian, Z. Ye, and B. Wu, "Online detection of broken rotor bars in induction motors by wavelet packet decomposition and artificial neural networks," *IEEE Trans. Instrum. Meas.*, vol. 58, no. 7, pp. 2253–2263, Jul. 2009.
- F. F. Costa, L. A. L. de Almeida, S. R. Naidu, and E. R. Braga-Filho, "Improving the signal data acquisition in condition monitoring of electrical machines," *IEEE Trans. Instrum. Meas.*, vol. 53, no. 4, pp. 1015–1019, Aug. 2004.
- E. C. C. Lau and H. W. Ngan, "Detection of motor bearing outer raceway defect by wavelet packet transformed motor current signature analysis," *IEEE Trans. Instrum. Meas.*, vol. 59, no. 10, pp. 2683–2690, Oct. 2010.
- Y. Da, X. Shi, and M. Krishnamurthy, "A new approach to fault diagnostics for permanent magnet synchronous machines using electromagnetic signature analysis," *IEEE Trans. Power Electron.*, vol. 28, no. 8, pp. 4104–4112, Aug. 2013.
- Y. Qi, E. Bostancı, M. Zafarani, and B. Akin, "Severity estimation of interturn short circuit fault for PMSM," *IEEE Trans. Ind. Electron.*, vol. 66, no. 9, pp. 7260–7269, Sep. 2019.
- T. Li *et al.*, "Simulation study on interturn short circuit of rotor windings in generator by RSO method," in *Proc. IEEE Int. Conf. High Voltage Eng. Appl. (ICHVE)*, Sep. 2018, pp. 1–4, doi: [10.1109/ICHVE.2018.8641917](https://doi.org/10.1109/ICHVE.2018.8641917).
- S. Uhrig, F. Öttl, R. Hinterholzer, and N. Augeneder, "Reliable diagnostics on rotating machines using FRA," in *Proc. Int. Conf. Diag. Electr. Eng. (Diagnostika)*, Sep. 2020, pp. 1–6, doi: [10.1109/Diagnostika49114.2020.9214647](https://doi.org/10.1109/Diagnostika49114.2020.9214647).
- C. A. Platero, F. Blázquez, P. Frías, and D. Ramírez, "Influence of rotor position in FRA response for detection of insulation failures in salient-pole synchronous machines," *IEEE Trans. Energy Convers.*, vol. 26, no. 2, pp. 671–676, Jun. 2011.
- F. R. Blánquez, C. A. Platero, E. Rebollo, and F. Blanquez, "Evaluation of the applicability of FRA for inter-turn fault detection in stator windings," in *Proc. 9th IEEE Int. Symp. Diag. Electr. Mach., Power Electron. Drives (SDEMPED)*, Aug. 2013, pp. 177–182, doi: [10.1109/DEMPE.2013.6645714](https://doi.org/10.1109/DEMPE.2013.6645714).
- F. R. Blánquez, C. A. Platero, E. Rebollo, and F. Blázquez, "Field-winding fault detection in synchronous machines with static excitation through frequency response analysis," *Int. J. Elect. Power Energy Syst.*, vol. 73, pp. 229–239, Dec. 2015.
- A. Mugarría, C. A. Platero, J. A. Martínez, and U. Albizuri-Txurruka, "Validity of frequency response analysis (FRA) for diagnosing large salient poles of synchronous machines," *IEEE Trans. Ind. Appl.*, vol. 56, no. 1, pp. 226–234, Jan./Feb. 2020.
- B. J. Small and A. Abu-Siada, "A new method for analysing transformer condition using frequency response analysis," in *Proc. IEEE Power Energy Soc. Gen. Meeting*, Jul. 2011, pp. 1–5, doi: [10.1109/PES.2011.6039470](https://doi.org/10.1109/PES.2011.6039470).
- M. Wang, A. J. Vandermaar, and K. D. Srivastava, "Improved detection of power transformer winding movement by extending the FRA high frequency range," *IEEE Trans. Power Del.*, vol. 20, no. 3, pp. 1930–1938, Jul. 2005.
- Z. Zhao, Y. Chen, Y. Yu, M. Han, C. Tang, and C. Yao, "Equivalent broadband electrical circuit of synchronous machine winding for frequency response analysis based on gray box model," *IEEE Trans. Energy Convers.*, vol. 36, no. 4, pp. 3512–3521, Dec. 2021.
- M. Pastura *et al.*, "Partial discharges in electrical machines for the more electric aircraft—Part I: A comprehensive modeling tool for the characterization of electric drives based on fast switching semiconductors," *IEEE Access*, vol. 9, pp. 27109–27121, 2021.
- S. Sundeep, J. Wang, and A. Griffó, "Holistic modeling of high-frequency behavior of inverter-fed machine winding, considering mutual couplings in time domain," *IEEE Trans. Ind. Appl.*, vol. 57, no. 6, pp. 6044–6057, Nov. 2021.

- [17] C. Yao *et al.*, "Noninvasive method for online detection of internal winding faults of 750 kV EHV shunt reactors," *IEEE Trans. Dielectr. Electr. Insul.*, vol. 22, no. 5, pp. 2833–2840, Oct. 2015.
- [18] V. A. Lavrinovich and A. V. Mytnikov, "Development of pulsed method for diagnostics of transformer windings based on short probe impulse," *IEEE Trans. Dielectr. Electr. Insul.*, vol. 22, no. 4, pp. 2041–2045, Aug. 2015.
- [19] Z. Zhao, C. Yao, N. Hashemnia, and S. Islam, "Determination of nanosecond pulse parameters on transfer function measurement for power transformer winding deformation," *IEEE Trans. Dielectr. Electr. Insul.*, vol. 23, no. 6, pp. 3761–3770, Dec. 2016.
- [20] K. Fukunaga, S. Okada, S. Ohtsuka, M. Hikita, and K. Kimura, "RPDIV/RPDEV characteristics of twisted-pair under repetitive bipolar impulse condition," in *Proc. Annu. Rep. Conf. Electr. Insul. Dielectr. Phenomena*, 2007, pp. 196–199, doi: [10.1109/CEIDP.2007.4451612](https://doi.org/10.1109/CEIDP.2007.4451612).
- [21] P. Wang, A. Cavallini, G. C. Montanari, and G. Wu, "Effect of rise time on PD pulse features under repetitive square wave voltages," *IEEE Trans. Dielectr. Electr. Insul.*, vol. 20, no. 1, pp. 245–254, Feb. 2013.
- [22] *Frequency Response Analysis on Winding Deformation of Power Transformers*, Chinese Standard DL/T 911-2016, 2016.
- [23] M. Florkowski and J. Furgat, "A high-frequency method for determining winding faults in transformers and electrical machines," *Rev. Sci. Instrum.*, vol. 76, no. 11, pp. 114701–114707, Nov. 2005.
- [24] H. Li, M. Zhao, D. W. Xiang, and H. Yan, "Online monitoring of incipient turn insulation deterioration of servo motor using switching transient frequency response," (in Chinese), *Proc. CSEE*, vol. 40, no. 10, pp. 3359–3368, May 2020.



Yueqiang Yu was born in Nanchong, Sichuan, China, in 1994. He is currently pursuing the master's degree with the Department of Electrical Engineering, College of Engineering and Technology, Southwest University, Chongqing, China.

His areas of research include condition monitoring and fault diagnosing for machine.



Zhongyong Zhao (Member, IEEE) was born in Guangyuan, Sichuan, China. He received the B.S. and Ph.D. degrees in electrical engineering from Chongqing University, Chongqing, China, in 2011 and 2017, respectively.

He received a scholarship from China Scholarship Council to enable him to attend a joint-training Ph.D. program in Curtin University, Perth, Western Australia, in 2015–2016. He is currently an Associate Professor in the College of Engineering and Technology, Southwest University, Chongqing, China. His areas of research include condition monitoring and fault diagnosing for HV apparatus, and artificial intelligence.



Yu Chen was born in Wenzhou, Zhejiang, China, in 2000. He is currently pursuing the bachelor's degree with the Department of Electrical Engineering, College of Engineering and Technology, Southwest University, Chongqing, China.

His areas of research include condition monitoring and fault diagnosing for power transformer, and application of artificial intelligence.



Hanzhi Wu was born in Qingdao, Shandong, China, in 2000. He is currently pursuing the bachelor's degree with the Department of Electrical Engineering, College of Engineering and Technology, Southwest University, Chongqing, China.

His areas of research include condition monitoring and fault diagnosing for electric machinery, and application of artificial.



Chao Tang (Member, IEEE) was born in Sichuan, China, in 1981. He received the M.S. and Ph.D. degrees in electrical engineering from Chongqing University, Chongqing, China, in 2007 and 2010, respectively.

As a Ph.D. student (2008–2009) and as a Visiting Scholar in 2013 and (2015–2016), he studied with the Tony Davies High Voltage Laboratory, University of Southampton, U.K., doing some researches on the dielectric response characteristics and space charge behaviors of oil-paper insulation. He is currently a Professor with the College of Engineering Technology, Southwest University, Chongqing, China. His research interests include mainly in the field of on-line monitoring of insulation conditions and fault diagnosis for high-voltage equipment.



Wenwen Gu was born in Chongqing, China, 1983. She received the B.S. and Ph.D. degrees in electronics science and technology and instrument science and technology from Chongqing University, Chongqing, China, in 2006 and 2012, respectively.

She is currently an Associate Professor in the College of Engineering and Technology, Southwest University, Chongqing. Her areas of research include microelectromechanical systems and fault diagnosing.